Lagrangian acceleration measurements at large Reynolds numbers

Greg A. Voth, K. Satyanarayan, and Eberhard Bodenschatz[a)]
Laboratory of Atomic and Solid State Physics, Cornell University, Ithaca, New York 14853-2501

(Received 4 November 1997; accepted 5 May 1998)

We report experimental measurements of Lagrangian accelerations in a turbulent water flow between counter-rotating disks for Taylor–Reynolds numbers $900<R_\lambda<2000$. Particle tracks were recorded by imaging tracer particles onto a position sensitive photodiode, and Lagrangian information was obtained from fits to the position versus time data. Several challenges associated with extracting Lagrangian statistical quantities from particle tracks are addressed. The acceleration variance is obtained as a function of Reynolds number and shows good agreement with Kolmogorov (1941) scaling. The Kolmogorov constant for the acceleration variance is found to be $a_0=7\pm3$. © *1998 American Institute of Physics.* [S1070-6631(98)00809-5]

I. INTRODUCTION

An understanding of Lagrangian statistics is of great importance in the ongoing effort to develop both fundamental and practical descriptions of turbulence. This was recognized already in 1921 by Taylor in his seminal paper on turbulent diffusion,[1] but almost no studies of Lagrangian turbulence quantities at large Reynolds numbers have been performed. The primary reason for this has been the lack of tools for measuring or calculating Lagrangian statistics at large Reynolds numbers.

From a fundamental point of view, high Reynolds number Lagrangian turbulence data is needed to provide a new perspective from which to judge Kolmogorov's 1941 theory. A host of practical applications follow from the connection to turbulent diffusion. Lagrangian stochastic models are widely used for simulating turbulent flows in which transport is of primary interest. Examples include turbulent combustion[2] and pollutant transport in the atmosphere.[3] These models are often applied at Reynolds numbers much larger than existing data, and so model constants are unknown.

Determining particle accelerations in a turbulent flow has long been recognized as a difficult problem. At large Reynolds numbers, particles are typically moving at high speeds along erratic trajectories whose accelerations are only correlated over times on the order of the Kolmogorov time scale.[4] In this situation, accurate acceleration measurements require high resolution, extremely high speed imaging equipment. Previous work had typically relied on pixel based video photography, and this resulted in pessimism above ever being able to measure the small scale Lagrangian properties of high Reynolds number turbulence.[5]

In this paper we present experimental particle tracking measurements in a flow between counter-rotating disks for Taylor–Reynolds numbers $900<R_\lambda<2000$, an order of magnitude higher than previously possible. We recorded particle tracks by imaging tracer particles onto a position sensitive photodiode, and obtained data with sufficient spatial and temporal resolution to measure accelerations. We report data on the velocity and acceleration statistics and discuss challenges in the data analysis. Our results for the acceleration variance as a function of Reynolds number are in excellent agreement with Kolmogorov's (1941) scaling predictions and as such provide the first evidence that at sufficiently large Reynolds numbers, Lagrangian acceleration statistics can be described by Kolmogorov scaling.

A. Lagrangian Kolmogorov scaling

Kolmogorov's 1941 hypotheses[6] yield predictions for the scaling of several Lagrangian statistics that have never been tested. Following the notation of Monin and Yaglom,[7] the second-order Lagrangian velocity structure function is defined as

$$D_{ij}^{L(2)}(\tau)=\langle(u_i(t+\tau)-u_i(t))(u_j(t+\tau)-u_j(t))\rangle, \quad (1)$$

where u_i and u_j are components of the velocity vector of a fluid particle and τ is a time difference. If the flow is statistically stationary and $\tau\ll T_L$, where T_L is the Lagrangian velocity correlation time scale, Kolmogorov's hypotheses predict that at sufficiently high Reynolds number

$$D_{ij}^{L(2)}(\tau)=(\epsilon\nu)^{1/2}\beta(\tau/\tau_\eta)\delta_{ij}, \quad (2)$$

where ϵ is the mean dissipation per unit mass, ν is the kinematic viscosity, $\tau_\eta\equiv(\nu/\epsilon)^{1/2}$ is the Kolmogorov timescale, and $\beta(\tau/\tau_\eta)$ is a universal function. Furthermore, in the inertial time range where $\tau\gg\tau_\eta$, this result must be independent of ν and one obtains

$$D_{ij}^{L(2)}(\tau)=C_0\epsilon\tau\delta_{ij}, \quad (3)$$

where C_0 is a universal constant. Similarly, for the higher order structure functions in the inertial time range

$$D^{L(p)}(\tau)\sim(\epsilon\tau)^{p/2}. \quad (4)$$

a)Electronic mail: eb22@cornell.edu

(For odd orders, $D^{L(p)}$ is zero by symmetry unless the absolute value of the velocity difference is used.)

Predictions for the moments of the fluid particle acceleration probability density function (PDF) can be obtained by assuming that $u_i(t)$ is differentiable and taking the limit $\tau \to 0$ of the Lagrangian velocity structure functions. In particular, the second-order structure function scales as τ^2 for small τ yielding the prediction for the acceleration variance

$$\langle a_i a_j \rangle = a_0 \epsilon^{3/2} \nu^{-1/2} \delta_{ij}, \tag{5}$$

where a_0 is another universal constant. The analysis that led to Eq. (5) can also be extended to the higher moments of the acceleration distribution, and it is found that Kolmogorov's 1941 hypotheses predict that the normalized acceleration moments should be constants

$$\frac{\langle a^p \rangle}{\langle a^2 \rangle^{p/2}} = a_p. \tag{6}$$

Note that the acceleration variance is the Lagrangian counterpart to the mean dissipation in the Eulerian perspective. Equation (5) can be viewed as predicting that the Lagrangian quantity, $\nu^{1/2}\langle a_i a_i \rangle$, is similar to the mean dissipation. It is a characteristic of the small scales yet its magnitude is determined by the large scales, and hence it is independent of viscosity. In some ways, this is a natural quantity to use for Lagrangian Kolmogorov scaling in place of the dissipation. The measurements presented in this paper support the idea that the two scales are indeed related as predicted in Eq. (5).

Continuing the analogy with Eulerian results, it is expected that intermittency will cause deviations from the predictions for the higher acceleration moments and the higher order structure functions. Measurements of these quantities could lead to an important new perspective from which to study intermittency.

B. Prior work

Experimental Lagrangian measurements have been of three distinct types. The first measurements used Taylor's 1921 theory[1] of turbulent dispersion to determine the Lagrangian velocity correlation function from the scalar dispersion. Shlien and Corrsin[8] provided a summary of measurements using this technique before themselves offering a set of measurements.

The second technique was optically tracking tracer particles that approximated Lagrangian motion. Snyder and Lumley[9] provided the first systematic set of particle tracking velocity measurements from wind tunnel grid turbulence. Sato and Yamamoto[10] have reported similar measurements in water tunnel grid turbulence. Virant and Dracos[11] have developed a stereoscopic system for measuring many particle tracks at once in three dimensions and report measurements in a turbulent boundary layer. Each of these studies has been helpful in illuminating the large scale Lagrangian properties of turbulence, but resolution limits and low Reynolds numbers have precluded comparison of small scale statistics with Kolmogorov's ideas.

The third technique has been to use the relations between the fourth-order velocity structure functions and pressure structure functions[12–14] to calculate pressure gradient statistics from hot wire velocity measurements. This allows measurement of particle accelerations since the acceleration of fluid particles is dominated by the pressure gradient contribution for all but the smallest Reynolds numbers. This was originally suggested by Obukhov and Yaglom[12] and Batchelor,[13] and has recently been convincingly demonstrated in DNS by Yeung.[15] Hill and Thoroddsen[16] have used this technique to study spatial acceleration correlations at $R_\lambda = 208$. Spatial resolution limitations kept them from reporting one point acceleration statistics.

The only available high Reynolds number data came from balloon tracking in the atmospheric boundary layer.[17] These data roughly support the linear scaling of the Lagrangian velocity structure function in the inertial range [Eq. (3)] and the value of C_0 is 4.0 ± 2.0. Unfortunately, the small sample size and variable flow conditions limited the conclusions that could be drawn.

In addition to experiments, there have been several direct numerical simulations (DNS) of Lagrangian statistics of turbulence. Much as in the Eulerian case, DNS has provided unparalleled accuracy but has been limited to $R_\lambda < 200$. Yeung and Pope[4] provided a comprehensive study of Lagrangian statistics in artificially forced isotropic homogeneous turbulence. Squires and Eaton[18] calculated statistics of homogeneous shear flows. More recently Yeung has studied two particle Lagrangian statistics[19,20] and has extended the one-particle results to $R_\lambda = 200$.[15] A clear conclusion of these studies is that the acceleration variance is not scaling as predicted in Eq. (5) for $R_\lambda < 200$.

II. EXPERIMENTAL SETUP AND METHODS

In this work we are reporting results on particle velocities and accelerations obtained by optically tracking tracer particles. The method is conceptually straight forward. The flow is seeded with small neutrally buoyant tracer particles and a portion of the flow is illumined by a light source. The illumined region is imaged onto a device to record tracer particle position as a function of time. In this way a two-dimensional projection of the trajectory is obtained. As long as the tracer particles are sufficiently small to approximate fluid elements, Lagrangian velocities and accelerations can be calculated as derivatives of the particle positions.

A. The flow between counter-rotating disks

The flow we used was water driven between two counter-rotating disks in a closed cylindrical container of moderate volume (110 liters). This flow has recently attracted much attention because it allows very high Reynolds numbers in a confined environment.[21–25] The effects of the recirculating inhomogeneous flow are potentially a concern for large scale statistics, but for the dissipation scales at the Reynolds numbers attained it seems reasonable to expect that this will not be a problem.

A picture and schematic of the apparatus are shown in Fig. 1. It consisted of a cylindrical container made of plexiglass (PMMA) with hard anodized aluminum top and bottom plates. The setup could be temperature controlled by water

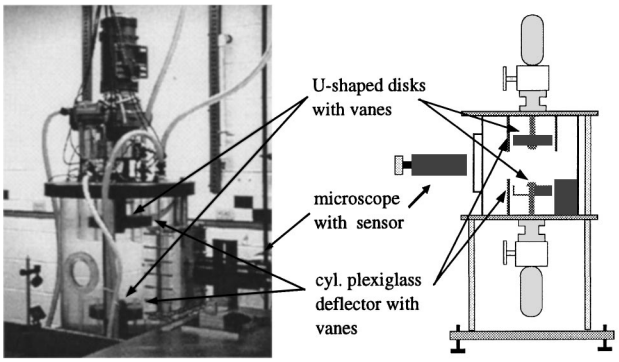

FIG. 1. Picture and schematic of the experimental apparatus. In the schematic the lower part shows a cut through the U-shaped disc and the deflection cylinder. At the right the vanes can be seen.

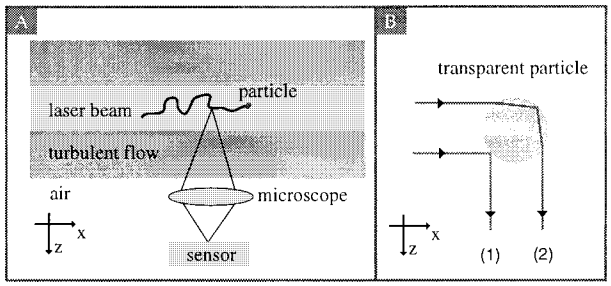

FIG. 2. (A) Schematic of the optical setup and (B) of the primary (1) and secondary (2) reflections from the transparent spheres.

running through channels in the plates. The transparent cylindrical shell had a diameter of 48.3 cm and a height of 60.5 cm. A large plane window was mounted on the side to allow undistorted visualization, and a smaller circular, plane window was mounted at 90° for illumination. The two circular disks of 20.3 cm diameter had U-shaped cross sections with height of 4.3 cm and were mounted to 5 cm diameter shafts that were connected to the external drive. Twelve equally spaced vanes were mounted in each disk to provide efficient stirring. The disks were spaced 33 cm apart. Both the disks and the shafts were machined from aluminum and hard anodized for corrosion resistance. The disks were surrounded by a stationary, cylindrical, plexiglass deflector shield of 25.4 cm diameter which extended 5 cm beyond the disks. These deflectors confined the turbulence to the central region of the apparatus. They also had vanes that extended to the edge of the apparatus which damped out any large scale rotation caused by slight mismatch in the disk speeds. The disks were driven by two electronically controlled 0.9 kW dc motors, which were geared down by a variable speed reducer. The disk rotation frequency was measured optically by an LED/photodiode pair and was feedback controlled to 0.1% long term stability with the fluctuations due to the turbulence being less than 1%. The apparatus was vacuum tight and allowed a thorough degassing of the fluid to eliminate bubbles. The fluid was filtered to particle sizes <0.3 μm, and the relatively small volume made it possible to maintain excellent chemical purity.

B. Detection system

For illumination of the detection region, a 5 W continuous wave argon ion laser beam was used which produced a cylindrical illumination volume that passed horizontally (along the x axis) through the center of the cell. The laser beam had a Gaussian profile with a width of 1 mm, and was polarized in the y direction. A 1.5 mm section of the beam was viewed from 90° (along the z axis) at a distance of 30 cm by a long working distance microscope. The image was focused onto a position sensitive photodetector. This is shown schematically in Fig. 2(A).

The detector was essentially a large square photodiode (1.0 cm on a side) which allowed an analog two-dimensional measurement of the position of a single light spot. It works by measuring the fraction of the photocurrent that migrates to the top versus bottom of the front plane, and to the right versus left of the back plane. Each of the four leads was connected to a charge sensitive amplifier and signals from two opposing sides were added and subtracted in analog. The resulting signals were digitized and stored by a 4-channel digital oscilloscope. The waveforms were acquired at a 250 MHz digitization rate. Positions were only needed at typically 100 kHz, so 2500 samples were averaged at each point to reduce the noise. The resulting waveforms were transferred via the GPIB bus to a Pentium computer where they were stored. Positions were calculated later by a division of the corresponding difference and sum waveforms. The time interval between recorded tracks was limited to 0.5 s by the data transfer rate through the GPIB bus. The detector was carefully checked for linearity of its position output by scanning a fiber optic over its surface. It was linear to better than 1% over the central 70% of its length in both the horizontal (x) and vertical (y) directions. To minimize position measurement error, only positions which were within this central region were used in the data analysis.

After an experiment, the position scale of the detection system was calibrated by moving the unchanged system (microscope and detector) from the turbulence chamber to an aquarium of the same optical geometry. The end of a multimode optical fiber was attached to a micrometer and was positioned within the water in the focus of the microscope. The positions of the light spot were recorded as the fiber optic was moved. With this technique we obtained a calibration of the position scale within $\pm 2\%$.

C. Particles

For tracer particles, we used transparent polystyrene spheres with density 1.06 g/cm^3. The concentration of particles was kept low and was chosen to give one particle track every 1 to 2 s. For the particles to follow the flow passively one would like to minimize their size. In our experiment the minimal size was dictated by the need to gather enough light for the detector to give sufficiently accurate position measurements. We used two different diameter particles. One batch had mean diameter of 250 μm taken from a 150 to 350 μm sieve cut. The other had a mean diameter 450 μm with standard deviation of 8 μm.

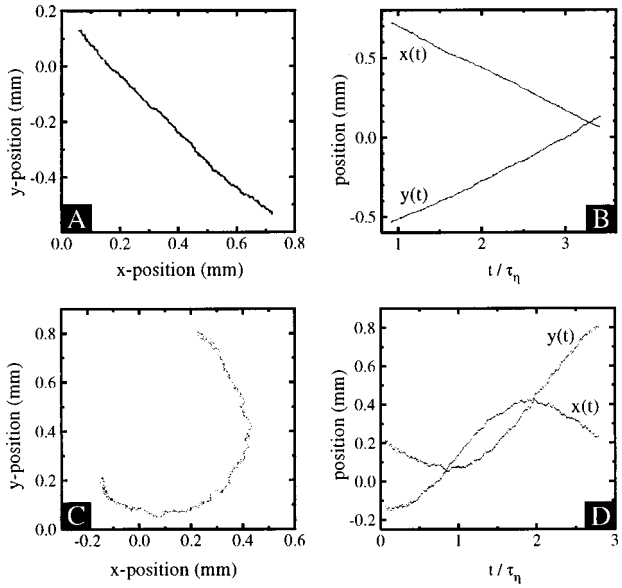

FIG. 3. Two examples particle tracks for run 9 with $\tau_\eta = 0.59$ ms and $\eta = 23$ μm. The upper trajectory represents a typical acceleration (at the center, $a_y = 90$ m/s^2, half the rms acceleration), while the lower track represents a rare event (at the center, $a_y = 1490$ m/s^2, 8 times the rms). Both the particle trajectories (A)&(C) and the positions vs time (B)&(D) are shown.

We also tried to use higher reflectivity, silver coated, hollow glass spheres. These spheres would have had the advantage that smaller particles could have been used. However, experiments showed that the reflective surface of the particles was very inhomogeneous. As the particles rotated, the inhomogeneous reflectivity of the particles' surface led to rapid fluctuation in the reflected light intensity. Due to the relatively slow response time of the position sensitive photodiode (2 μs), these rapid fluctuations could not be resolved and resulted in inaccurate position measurements. In an attempt to overcome this problem we also used a position sensitive photomultiplier tube. Although this sensor had high light sensitivity and an ultrafast response time of 1 ns, its spatial resolution was not sufficient.

D. Particle tracks

Figure 3 contains two example particle tracks. The majority of the tracks recorded were almost straight like the one shown in Figs. 3(A) and 3(B), but a few displayed large curvature such as the one shown in Figs. 3(C) and 3(D). These sharply curved tracks suggest the expected intermittency of Lagrangian accelerations, and may be connected to the coherent structures which have recently attracted much interest.[23,24,26]

In the data analysis, random and systematic errors of the measured particle position data had to be considered. The accuracy of the position measurements was sensitively dependent on the intensity of the light gathered onto the detector. Due to the Gaussian intensity profile of the laser beam, a trajectory typically spanned a range of intensities and correspondingly a range of measurement uncertainties. To obtain an estimate of the magnitude of the random measurement error as a function of intensity, we fitted a polynomial to each trajectory assuming constant error. For each data point, the residual was calculated and registered with the point's light intensity. Repeating the same procedure for all trajectories, we obtained the rms residual as a function of intensity; and this was used as the position measurement error. The order of the fit polynomial was chosen to be $1 + t_\ell / \tau_\eta$, truncated to an integer, where t_ℓ is the total time the particle was tracked, and τ_η is determined in Sec. V C. This form was determined by studying the mean square deviation of fits as a function of track length for tracks generated by the Lagrangian stochastic model described in Sec. V B.

In addition to random position errors, we identified at least two types of systematic errors in the data. One occurred when multiple particles came into view at the same time. This resulted in sudden variations in the particle position, as the detector provided only the ''center of mass'' position of the light hitting it. We observed these tracks only rarely, since the time between detections was a factor of 500 longer than the time it took a particle to pass through the observation volume. Most of these tracks could be rejected on the basis of the nearly discontinuous position and velocity. Along the laser beam direction (the x axis), the transparent particles led to two reflections. This is shown schematically in Fig. 2(B). The larger horizontal size of the light spot increased the random uncertainty in the measured x position. It also had a systematic effect when one of the reflections was shadowed by another particle that passed through the laser beam outside of the observation volume. This shadowing effect led to trajectories where the particle suddenly appeared to have moved. Fortunately, this did not appear in the y data and it was simple to estimate its effect.

Another possible source of error was the nonuniformity of the polystyrene particles. Scratches and dents in the surface, deviations from a spherical shape, and index of refraction variations within the sphere would lead to changes in the position of the light spot produced by rotating particles, and thus to an error in the particle position measurements. While viewing the particles under a microscope, it did not appear that these effects should be large. However, this might contribute to the correlated errors discussed in Sec. V A.

III. DATA

The data sets presented in this paper were all recorded with the detection region at the zero mean velocity point at the center of the flow. We adjusted the detection system to the point that gave zero mean velocity, since we were able to measure the mean velocities with better spatial resolution than we could determine the geometric center of the flow. Position in the unmeasured z direction was set to our best determination of the geometric center of the flow—which should be the zero mean velocity location to within about 5 mm.

Each data set consists of a large number of tracks with 500 position measurements per track. Because particles remained in the detection region for varying time periods, the valid part of each track was some fraction of the total 500 points. Data were acquired at about 5000 tracks per hour.

TABLE I. Parameters for all runs.

Run	f (Hz)	$\tilde{u}$ (m/s)	R_λ	ν (10^{-6} m^2/s)	ϵ (m^2/s^3)	τ_η (ms)	η (μm)	t_m/τ_η	N_{tr}
250 μm particles									
1	2.50	0.281	985	0.91±0.01	0.106	2.93	52	1.7	15211
2	2.50	0.281	921	1.04±0.02	0.106	3.14	57	1.6	11910
3	3.75	0.419	1180	0.95±0.05	0.351	1.64	39	3.0	22000
4	3.75	0.419	1147	1.00±0.02	0.351	1.69	41	3.0	26870
5	5.00	0.546	1338	0.96±0.03	0.777	1.11	33	4.5	8499
6	5.00	0.571	1340	1.00±0.02	0.887	1.06	33	1.9	8318
7	6.25	0.689	1499	0.97±0.02	1.58	0.78	27	2.6	18764
8	6.25	0.693	1503	0.97±0.02	1.55	0.79	28	6.3	15077
9	7.50	0.834	1668	0.94±0.02	2.76	0.59	23	3.4	28790
10	9.50	1.063	1981	0.85±0.02	5.72	0.39	18	5.3	8132
11	9.50	1.060	2004	0.83±0.02	5.67	0.38	18	5.3	12579
460 μm particles									
12	2.50	0.280	1011	0.86±0.01	0.104	2.88	50	1.7	3962
13	3.75	0.419	1236	0.86±0.01	0.351	1.57	37	3.2	6134
14	5.00	0.559	1410	0.88±0.01	0.832	1.03	30	4.9	7995
15	5.00	0.559	1410	0.88±0.01	0.832	1.03	30	9.7	13056
16	6.25	0.693	1595	0.86±0.02	1.57	0.74	25	2.7	13994
17	7.50	0.834	1777	0.84±0.01	2.80	0.55	21	3.7	13965
18	9.50	1.060	2021	0.82±0.01	5.69	0.38	18	5.3	13156

The maximum Reynolds number studied was limited by the power available from the motors. The minimum Reynolds number was limited by the necessity of keeping enough particles suspended in the flow. For small fluctuating velocities, the particles settled out of the inactive regions in the flow; and thus sufficient statistics could not be collected at lower Reynolds numbers.

Parameters for all data sets are given in Table I. Each run is identified by a number. The rotation frequency of the disks is f. The typical velocity used for scaling is $\tilde{u}=(\langle u_i u_i\rangle/3)^{1/2}$ where the unmeasured velocity component (u_z) is assumed to have the same statistics as the measured horizontal component (u_x) due to the cylindrical symmetry. For the 460 μm particles, the error in the x position measurements were too large to determine accurate x velocities. The y velocities were very similar to the values for the smaller particles, so we set $\tilde{u}$ for the larger particles equal to the average of the velocities of the smaller particles at the same frequency.

We determined the dissipation by

$$\epsilon=\tilde{u}^3/L, \tag{7}$$

where $L=0.21$ m includes the normal constant coefficient in this equation and is determined from the form of the acceleration autocorrelation function in Sec. V C. For the Taylor microscale Reynolds number, we used the usual isotropic definitions

$$R_\lambda=\frac{\tilde{u}\lambda}{\nu}=\left(\frac{15\tilde{u}L}{\nu}\right)^{1/2}, \tag{8}$$

since

$$\lambda=\left(\frac{15\nu\tilde{u}^2}{\epsilon}\right)^{1/2}. \tag{9}$$

The kinematic viscosities given are for the mean temperature of each run, with the uncertainty reflecting temperature drift. Values were obtained from Ref. 27. The Kolmogorov scales of time and length are $\tau_\eta=(\nu/\epsilon)^{1/2}$ and $\eta=(\nu^3/\epsilon)^{1/4}$, respectively; t_m is the maximum tracking time, which is determined by the time base setting on the oscilloscope; N_{tr} is the number of tracks with more than 25 positions recorded.

IV. MEASURING VELOCITY STATISTICS

Measurements of the mean velocity and rms velocity fluctuations are essential in describing the turbulent flow. As with almost all known fluid measurement techniques, it is nontrivial to extract these statistical quantities from the raw data. Just as in burst laser Doppler anemometry (LDA), the probability of a particle being observed depends on its velocity; thus the naive velocity moments calculated by sums over observed particle velocities are incorrect. Buchave *et al.*[28] provided an analysis of the basic issues and a method of calculating the corrected velocity moments using particle transit (residence) times.

We have developed a different but equivalent method based on the form of the velocity probability density function (PDF). The motivation for this was twofold:

(i) The data acquisition procedure applied here and described above did not allow the measurement of residence times for all tracks, i.e., some slow particles stayed in the detection region longer than the digitization time. This made it impossible to use the method discussed by Buchave *et al.*[28]

(ii) The PDF method opens the door to Monte Carlo modeling of the detection process. By using Lagrangian stochastic models one can simulate tracks from which one can calculate the PDF for detecting a particle conditional on its velocity vector. As shown below, this conditional PDF can be used to calculate the true PDF of the velocity. It should be

possible to apply this method to other situations where the residence time method is not easily applicable. Examples would be where the detection region is large or oddly shaped, or multiple particles are tracked at once. For the purposes of this paper, the use of Monte Carlo modeling was not necessary.

A. Correction of measurement biases in the velocity PDF

Let us define the correct three-dimensional joint velocity PDF to be $F_u(\mathbf{u})$. The measured PDF is given by the correct distribution conditional on a valid particle track being detected: $F_{u|D}(\mathbf{u}|D)$, where D can be thought of as a binomial random variable representing whether a particle is detected or not. The problem is to model the detection process so that a relationship between F_u and $F_{u|D}$ can be found. Our solution is to develop a model for $F_{D|u}(D|\mathbf{u})$ and then use Bayes' theorem to invert this to the desired form:

$$F_{u|D}(\mathbf{u}|D)=\frac{F_{D|u}(D|\mathbf{u})F_u(\mathbf{u})}{\int F_{D|u}(D|\mathbf{u}')F_u(\mathbf{u}')d^3\mathbf{u}'}. \tag{10}$$

There is a rich history of philosophical debate surrounding the application of this theorem to decision theory, but its use here as a means of inverting conditional probabilities is well accepted.[29]

In order to develop a model for $F_{D|u}(D|\mathbf{u})$, we assume:

(i) The detection region is small enough that velocity PDFs do not vary across it.

(ii) The velocity of a particle does not change significantly between entering the detection volume and the point where the velocity is measured.

(iii) The detection region is isotropic, so that its cross-sectional area does not depend on the velocity direction.

(iv) Particles are uniformly distributed in space with low enough density that the probability of multiple particles being detected is negligible.

(v) All particles that enter the detection region produce valid tracks.

This model corresponds well to the situation in our flow. Assumption (i) was clearly valid across the 1 mm^3 detection region. Assumption (ii) was fairly good since measurements given later showed that changes in velocity were typically less than 15%, and they were this large only for the largest Reynolds numbers. By changing the point along the track at which the velocity was sampled, we determined that this effect was not significant. Assumption (iii) was probably the weakest since the detection region was a cylinder. However, the geometry used in the experiment was still reasonably approximated by a sphere. With our enclosed turbulent flow and maximum data rates of two measurements per second (iv) was satisfied. Assumption (v) is difficult to quantify. Some particles will pass through the corners of the region and their tracks will not have enough points to fit a velocity. This could lead to a bias against large velocities, but should not be a large effect.

With these assumptions, the rate of particles passing through a spherical detection region of cross-sectional area ΔS is

$$R=|\mathbf{u}|n\Delta S, \tag{11}$$

where n is the number of particles per unit volume. In this situation, the PDF of the number of particles detected in a time interval Δt, conditional on the velocity, is a Poisson distribution. With small particle densities and short particle transit times, only the probability of one particle is significant, and it simplifies to

$$F_{D|u}(D|\mathbf{u})=R\Delta t=|\mathbf{u}|n\Delta S\Delta t. \tag{12}$$

Inserting this into Bayes' theorem gives

$$F_{u|D}(\mathbf{u}|D)=\frac{|\mathbf{u}|n\Delta S\Delta tF_u(\mathbf{u})}{\int|\mathbf{u}'|n\Delta S\Delta tF_u(\mathbf{u}')d^3\mathbf{u}'}, \tag{13}$$

and thus the measured distribution is related to the correct one by

$$F_{u|D}(\mathbf{u}|D)=K|\mathbf{u}|F_u(\mathbf{u}), \tag{14}$$

where K is a normalization constant. With Eq. (14) the correct PDF can be calculated from the full three-dimensional measured distribution.

The method described above is equivalent to the method of residence time weighting described by Buchave *et al.*[28] We show this for the mean velocity, since the higher moments of the velocity distribution can be shown to agree in the same way. They obtain the mean velocity by a residence time weighted average of the sampled velocities

$$\overline{u}_i=\frac{\Sigma_k u_i^{(k)}\Delta t^{(k)}}{\Sigma_k\Delta t^{(k)}}, \tag{15}$$

where $u_i^{(k)}$ is the kth measurement of the velocity component i, and $\Delta t^{(k)}$ is the time over which the kth particle traverses the observation volume. In PDF notation, the equivalent quantity is

$$\overline{u}_i=\frac{\int u_i\Delta tF_{u|D}(\mathbf{u}|D)d^3\mathbf{u}}{\int\Delta tF_{u|D}(\mathbf{u}|D)d^3\mathbf{u}}. \tag{16}$$

Now substitute $F_{u|D}(\mathbf{u}|D)$ from Eq. (14) and recognize that Δt is just $\ell/|\mathbf{u}|$, where ℓ is the distance the track travels. Since ℓ is independent of the velocity, we find

$$\overline{u}_i=\int u_iF_u(\mathbf{u})d^3\mathbf{u}. \tag{17}$$

Thus we see that residence time weighting of samples from the PDF in Eq. (14) produces the correct velocity moments.

B. Velocity data analysis and results

Our primary measurements are made in the zero mean velocity region at the center of the cylindrically symmetric flow. The statistics of the unmeasured z velocity component should be the same as for the measured x component because of the cylindrical symmetry. In addition, the Reynolds stresses should be zero at this location due to symmetry.

We measured the statistics of the x and y components of the particle velocities from linear fits to the center 25 points of each recorded track. The x and y projections of the measured joint velocity PDF for run 9 is shown in Fig. 4. The

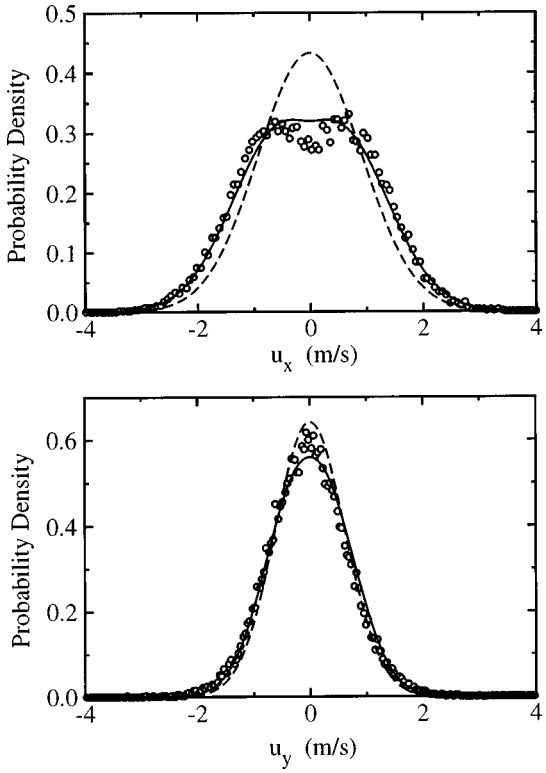

FIG. 4. PDF of the x and y component of the measured velocities, computed from linear fits to particle tracks for run 9. Also shown is the fit using Eq. (18) (solid) and the true velocity PDF after bias correction (dashed).

Reynolds stress between the x and y velocity components was zero to within the measurement resolution.

To correct for the biases discussed above, we were not able to apply Eq. (14) directly because we did not have measurements of the z velocity component. We circumvented this problem by assuming that the correct velocity PDF was a joint Gaussian. Far from the walls of high Reynolds number flows, velocity PDFs are known to be very nearly Gaussian with deviations which should not be perceptible in the second order moments which we need to determine.[30] With this information, Eq. (14) can be integrated over the unmeasured z direction to obtain the form of the joint PDF of the measured x and y velocities,

$$F^*_{u|D}(u_x,u_y|D)=K\int_{-\infty}^{\infty}|\mathbf{u}|\exp\left(-\frac{u_x^2}{2\sigma_x^2}-\frac{u_y^2}{2\sigma_y^2}-\frac{u_z^2}{2\sigma_x^2}\right)du_z, \tag{18}$$

where only σ_x and σ_y are fit parameters.

To determine these two unknown velocity standard deviations, we integrated Eq. (18) numerically and used a nonlinear least squares fitting routine to fit the model to the measured two-dimensional joint PDF.

Projections of the model fit to the measured PDF are shown in Fig. 4. The fitted values are $\sigma_x=0.921$ m/s and $\sigma_y=0.622$ m/s. The ratio of the rms velocity components is 1.48 which is typical of the values observed in homogeneous shear flows.[31] The model captured the measurement bias quite well, except that the fit slightly overestimated the probability for x velocities near zero. As a result, it appears that

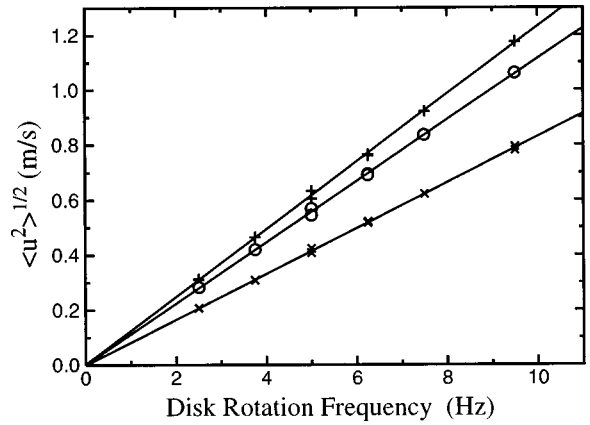

FIG. 5. Fluctuating velocities for runs 1 to 11. ○, $\tilde{u}$; +, σ_x; ×, σ_y. Solid lines are linear fits. The linear scaling demonstrates that there were no significant changes in the large scale structure of the flow.

the model slightly underestimated the rms x velocity. With the *ad hoc* assumption that the x and z velocity variances are different in Eq. (18), the model produces a considerably better fit to the central region of the x velocity PDF. Although this allowed a better fit, it only led to a 3% change in the fitted rms x velocity. Since it is likely that other approximations in the model and not lack of symmetry is causing the deviation, we fitted only for σ_x and σ_y and recognize a 3% uncertainty in the bias corrections.

The issue of measurement uncertainty in the measured velocity PDF should be addressed. The error contribution can be determined from plots of the standard deviation of the measured PDF versus the number of points used in the fit to estimate the velocity. These show that for the linear fits over 25 points there was a 1% standard deviation contribution due to velocity measurement error, and a 1% bias due to the faster tracks being less likely to stay in the detection region long enough to be included in the sample. These effects are individually small, and together they tend to cancel.

The typical velocity used for scaling of the results presented in this paper is $\tilde{u}=(\langle u_i u_i\rangle/3)^{1/2}$. Figure 5 shows that $\tilde{u}$, σ_x, and σ_y all scale linearly with the disk frequency. For each disk frequency, other than $f=7.5$, two independent measurements are plotted. The data points with the largest deviation from the linear scaling at $f=5$ have lower statistics than most of the runs (see Table I), and appear again as the largest deviations from Kolmogorov scaling in Fig. 12. The linear scaling is important in establishing that there were no changes in the large scale structure of the flow over the Reynolds numbers studied.

V. PARTICLE ACCELERATION MEASUREMENTS

The most challenging part of measuring particle accelerations in high Reynolds number turbulence is to obtain high enough spatial and temporal resolution on particle position measurements. With the analog positioning system described above, we obtained position resolution of typically 5 μm and temporal resolution up to 4 μs. In our flow, this was sufficient to allow accurate determination of the acceleration variance and the extraction of the general form of the accel-

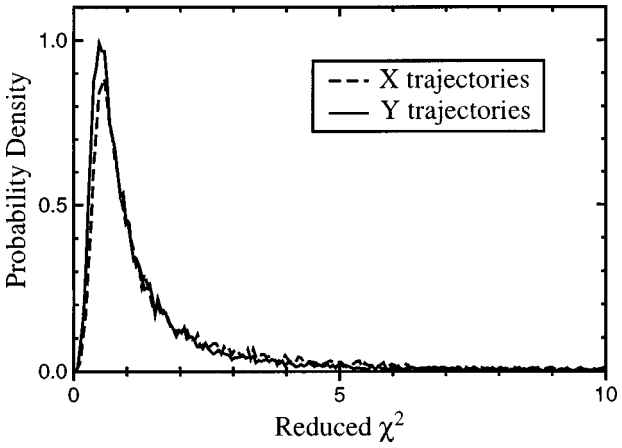

FIG. 6. Probability distributions of reduced χ^2 values of fits to position data from run 9. The slightly poorer fits of the x data may be attributed to the increased error due to double reflections as described in Sec. II D.

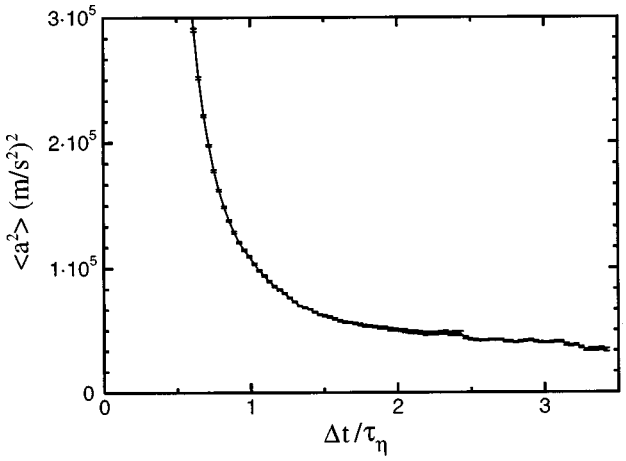

FIG. 7. Measured acceleration variance vs the trajectory time segment used in the fit. Data are for the y trajectories from run 9.

eration autocorrelation function. To distinguish between the true accelerations and the measurement errors, a rather involved data analysis was required which can be subdivided into three parts. In Sec. V A we describe the technique used to extrapolate the measured acceleration variance to eliminate the contribution from measurement errors. Section V B describes a method for correcting the systematic error introduced by fitting a second order polynomial to the trajectory. In Sec. V C we present a method for determining the dissipation ϵ from the acceleration correlation function. At several points, the data analysis required knowledge of a quantity that was determined in a later section. It was found that iterating the entire analysis twice was sufficient to provide self-consistency.

A. Extracting accelerations from particle tracks

The first step in extracting accelerations from particle trajectories was to eliminate the tracks that had large position measurement errors. This was done by fitting a polynomial to the entire track and eliminating tracks with large reduced χ^2 for the fit,[32] i.e., tracks with large rms deviation from the fit. Figure 6 shows the distribution of measured reduced χ^2 values. Particle tracks with a reduced $\chi^2>6$ were not considered for the data analysis. This cutoff resulted in about 4% of the y tracks and 7% of the x tracks being eliminated. Adjusting the cutoff down to 3 and up to 12 made only a 2% change in acceleration variance measurements, even though the measurement error contribution discussed later changed significantly. The order of the fit polynomial was chosen to be $1+t_\ell/\tau_\eta$, just as in Sec. II D. This procedure eliminates almost all the multiple particle and most of the shadowing effects discussed in Sec. II D.

After elimination of the spurious trajectories, a polynomial was fitted to a certain length of the track with the second time derivative giving the acceleration. As polynomial fitting is a linear operation, the acceleration obtained from the fit can be thought of as the acceleration of a fit to the true trajectory added to the acceleration of a fit to the measurement errors. The ideal situation would be to fit over a section of each track that was long enough that the acceleration due to the measurement errors would be negligible while still short enough that the polynomial was able to reproduce the trajectory. For our data the measurement errors were too large for this direct approach.

The technique we used to measure the acceleration was to fit second order polynomials to trajectory segments of size Δt centered around the midpoint of the trajectory—with Δt ranging from just a few points up to the entire tracking time. We repeated this procedure for all tracks in a run and thus obtained the acceleration variance as a function of trajectory time segment used in the fit. For very short trajectory segments, the measured acceleration variance was dominated by noise; while for increased segment length the noise contribution decreased. Very few particles were tracked for the longest segments, and consequently measurement uncertainty increased and eventually no variance could be measured. An example of this is shown in Fig. 7 for the y trajectories from run 9. The x trajectories were very similar except for a slightly larger noise contribution as described earlier in Sec. II D. The error bars were calculated by dividing the sample into eight sets, processing each set, and taking the standard deviation of the results from each set divided by the square root of the number of sets.

If the measurement errors were Gaussian and uncorrelated, the contribution to the acceleration variance from position measurement errors would be proportional to Δt^{-5}, where Δt is the time interval spanned by the evenly spaced points used in the fit.[33] In our case the errors were correlated and Δt^{-5} was not the correct form. However, the data for the square root of the measured acceleration variance were very nearly a constant added to a power law. This is equivalent to the variance having two error correlation lengths balanced such that

$$\langle a^2\rangle = A^2 + 2AB\Delta t^{-c/2} + B^2\Delta t^{-c}. \tag{19}$$

We used this power law to extrapolate to the true acceleration variance A^2.

It is very hard to determine the exact correlations in the measurement errors, so we cannot justify this form rigorously; but Eq. (19) provided excellent fits to the decay of the

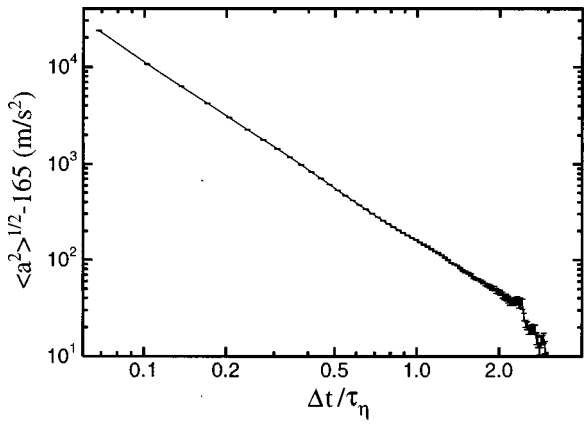

FIG. 8. Log-log plot of the square root of the acceleration variance with the fitted constant $A=165$ m/s^2 subtracted. The data are the same as for Fig. 7.

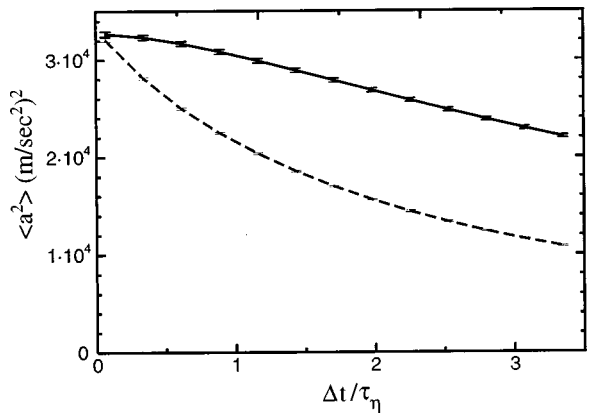

FIG. 9. Model calculation of the error in the acceleration variance due to underresolved trajectories. The dashed line is from direct application of Sawford's model. The solid line is from a modified model with differentiable particle accelerations.

measured acceleration variances with increased length of fitted trajectories. Fitted values of the exponent c were usually between 3 and 3.4. The log-log plot of the square root of the data in Fig. 8 with the fitted constant of $A=165$ m/s^2 subtracted, clearly shows that the noise contribution had power law behavior.

B. Acceleration measurement bias

A concern with the technique described above was that fitting a second order polynomial over several Kolmogorov timescales (see Table I) may not have captured the true accelerations, i.e., the quadratic polynomials might not have fully resolved the true trajectory structure and thus might have underestimated the acceleration variance. To quantify this effect, we developed a model to produce simulated stochastic particle tracks, and analyzed these tracks using the same code as in the data analysis of the experimental runs. Then we used the acceleration variances obtained from the model tracks to calculate the magnitude of the errors introduced by not fully resolving the experimental trajectories. These errors were later used in Sec. VI to correct for this effect.

The best model previously available for this is a second-order Lagrangian stochastic model developed by Sawford.[34,35] This model uses a continuous but nondifferentiable process to model the Lagrangian acceleration, and calculates velocities and positions from integrals of the accelerations. The dashed line in Fig. 9 shows the measured acceleration variance as a function of trajectory segment length when tracks from Sawford's model were analyzed. The extrapolation $t\to 0$ gives the true acceleration variance, which was an input parameter to the model. Figure 9 shows that our fitting procedure underestimated the acceleration variance, and that the error increased rapidly with increasing trajectory time segment. Yet from the fact that the error due to under-resolved trajectories goes linearly and not asymptotically to 0 for $t\to 0$, we concluded that the model was insufficient.

To improve on this, we modified Sawford's model. We applied it to the third time derivative of the position rather than to the acceleration. This new model produced trajectories with continuous, differentiable accelerations, and thus better captured the known form of the acceleration autocorrelation function. The new form of the model is

$$d\dot{a}_i(t) = -\left[1+\frac{\tau}{T_\infty}\right]\dot{a}_i(t)\,\frac{dt}{\tau} - \frac{a_i(t)}{T_\infty}\,\frac{dt}{\tau} + \left[2\langle \dot{a}_i^2\rangle\left(1+\frac{\tau}{T_\infty}\right)\right]^{1/2}\frac{dW}{\tau^{1/2}}, \tag{20}$$

where $\dot{a}_i(t)$ is the first time derivative of an acceleration component at time t. The rest of the notation is from the review by Pope.[35] The model constants, $\tau=0.5\tau_\eta$ and $T_\infty=0.7\tau_\eta$, were determined by fitting the acceleration autocorrelation function produced by the model to the Lagrangian DNS acceleration autocorrelation function from Yeung and Pope.[4] As explained in the next section, it is expected that the DNS results remain unchanged at higher Reynolds numbers. The input parameter, $\langle \dot{a}_i^2\rangle$, is determined by the curvature of the acceleration autocorrelation function at the origin to be

$$\langle \dot{a}_i^2\rangle = \frac{\langle a_i^2\rangle}{T_\infty \tau}, \tag{21}$$

where no summation is implied. For $\langle a_i^2\rangle$ we use the Kolmogorov prediction, Eq. (5), with $a_0=7$ as determined in Sec. VI.

This model produced better acceleration time series than Sawford's original model, but has nonstationary velocity statistics. For large scale properties this model is of little use, but it is a good approximation to the very short time behavior of a turbulent flow. Processing tracks from this model yielded the solid curve shown in Fig. 9.

The deviation between the solid line in Fig. 9 and the value for $t\to 0$ represents the bias introduced by fitting a second order polynomial over that trajectory time segment. In the final data analysis of the measured trajectories, we corrected for this bias by adding the modeled deviation onto

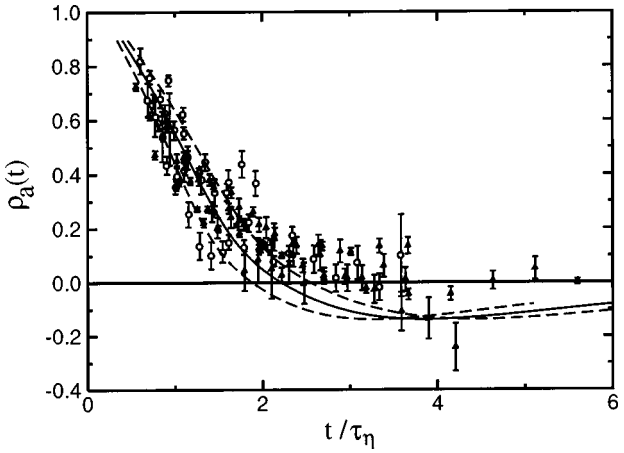

FIG. 10. Acceleration autocorrelation function for 250 μm particles (○); 460 μm particles (△); DNS data (see Ref. 4) (solid line); and estimated errors (dashed lines).

the measured acceleration for that length of trajectory segment (Fig. 7). Results both with and without this correction are given in Sec. VI.

C. Determining the dissipation from the acceleration autocorrelation function

The prevalence of turbulence research on flows with large mean velocities where Taylor's hypothesis may be applied can lead to the misconception that ϵ is always fairly simple to determine. In flows with zero mean velocity, which makes them attractive for Lagrangian studies, this is not the case.

We determine the mean dissipation from $\epsilon=\tilde{u}^3/L$, where $\tilde{u}$ is measured, and L is assumed to be determined by the geometry of the flow and independent of Reynolds number. To determine the value of L, we used a method[36] that relies on the autocorrelation function of an acceleration component, defined for the y component as

$$\rho_a(t)=\frac{\langle a_y(t_0)a_y(t_0+t)\rangle}{\langle a_y^2\rangle}. \tag{22}$$

Yeung and Pope[4] found from direct numerical simulations that, up to $R_\lambda=93$, $\rho_a(t)$ passed through zero at $t=2.2\tau_\eta$. For times smaller than this, the curves were essentially independent of Reynolds number when scaled by the Kolmogorov timescale. Yeung has recently found agreement with this at $R_\lambda=140$.[20] By measuring $\rho_a(t)$ for our data and scaling time so that it fell onto the known curve from Yeung and Pope,[4] we were able to determine the Kolmogorov timescale, τ_η, and from this, ϵ and L.

Figure 10 shows the acceleration autocorrelation function measured for the y component of all data sets with more than 10,000 tracks. The solid line is from Yeung and Pope[4] at $R_\lambda=93$. For each experimental run, $\rho_a(t)$ was determined by fitting second order polynomials to sections of each track separated by time t, multiplying the fitted accelerations and averaging over all tracks. Each autocorrelation function was normalized by the corrected acceleration variances given in Sec. VI. The time span used for the quadratic fits was chosen to be the time when the measured acceleration variance reached twice the extrapolated value for the sets with 460 μm particles and three times the extrapolated value for the sets with 250 μm particles (see Fig. 7). The results were surprisingly insensitive to the exact choice of time span, suggesting that the acceleration measurement errors were sufficiently uncorrelated. The error bars were determined as before by dividing each data set into segments and calculating the standard deviation between the segments divided by the square root of the number of segments. This made the incorrect assumption of Gaussian errors, so the errors were somewhat underestimated.

The observed collapse of the experimental data was obtained with the assumption that there was one constant length scale L in the flow. By using an arbitrary value for L, the dissipation can be determined from $\epsilon=\tilde{u}^3/L$ and thus τ_η. The ratios between the τ_η's for various data sets obtained in this manner were correct even though the overall magnitude of τ_η was arbitrary. Scaling the time axis for each data set by τ_η collapsed the data of all runs including both particle sizes, as shown in Fig. 10.

To determine the actual value of L, the time axis for all data sets together was scaled again to provide the best fit to the DNS results. This was done by a least-squares fit to the data for $\tau_\eta<2$. The value of L obtained from this least-squares fit was (0.21 ± 0.06) m. This value is very reasonable, as it is close to the diameter of the disks (0.203 m). We estimated the error in L by choosing limits that seemed visually reasonable. The dashed lines in Fig. 10 reflect the error estimates in L. They were found by scaling the simulation results by the amount corresponding to the error in L. The deviation between our data and the simulations for $\tau_\eta>2$ is expected. As the Reynolds numbers of the simulations increased, the negative excursion above $2.2\tau_\eta$ was continuously decreasing.[4] For the high Reynolds numbers in this experiment, the negative excursion should be very small and should extend to much longer times.

VI. RESULTS

Figure 11(A) shows $\nu^{1/2}\langle a_i^2\rangle$, where $\langle a_i^2\rangle$ is the variance of a single acceleration component, as a function of velocity scale for all of the data sets without applying the correction for underresolved trajectories (Sec. V B). The data clearly shows a power law. The prediction for the variance of fluid particle acceleration components from Kolmogorov's hypotheses is

$$\langle a_i^2\rangle=a_0\epsilon^{3/2}\nu^{-1/2}. \tag{23}$$

Using $\epsilon=\tilde{u}^3/L$, this can be rewritten

$$\nu^{1/2}\langle a_i^2\rangle=a_0L^{-3/2}\tilde{u}^{9/2}. \tag{24}$$

The scaling exponent of the data shown in Fig. 11(A) is in good agreement with the Kolmogorov prediction of $\tilde{u}^{9/2}$ shown by the solid line.

Figure 11(B) shows the same data with the underresolved trajectory correction applied. The correction raised the measured acceleration variance by amounts ranging from 3% up to 22%, depending on the typical number of Kolmog-

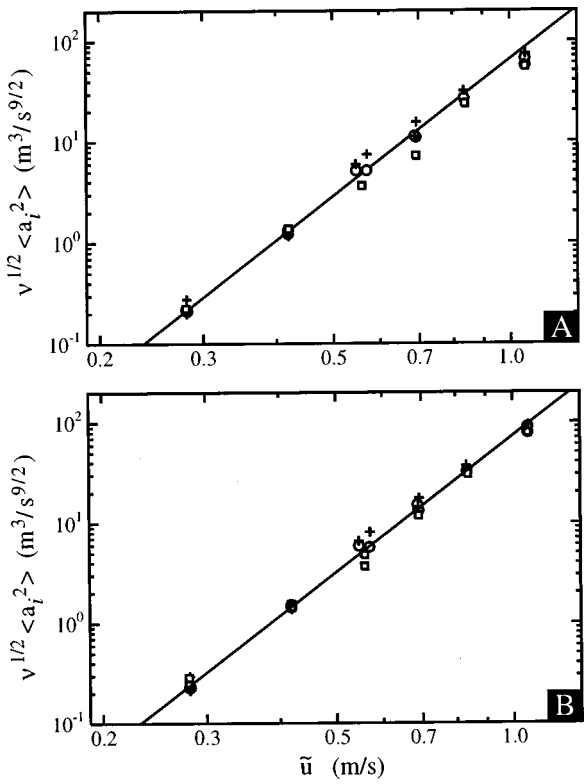

FIG. 11. Acceleration variance scaling; (A) raw data and (B) corrected for under-estimation of accelerations. y trajectories [250 μm (○) and 450 μm (□)] and x trajectories [250 μm (+)]. The solid line is the Kolmogorov $\tilde{u}^{9/2}$ prediction.

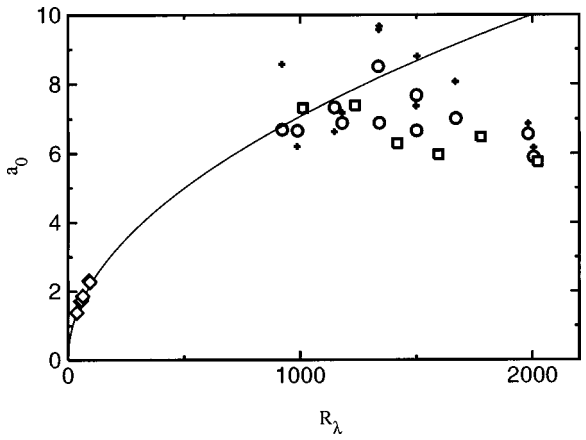

FIG. 12. Compensated acceleration scaling. y trajectories [250 μm (○) and 450 μm (□)] and x trajectories [250 μm (+)]. DNS data from Yeung and Pope (see Ref. 4) (◇).

orov timescales over which the particles were tracked. The agreement with Kolmogorov scaling is significantly improved. Over three orders of magnitude the scaling of the data with the smallest errors (the y data) is nearly indistinguishable from the predicted scaling. We emphasize that the agreement with Kolmogorov scaling requires only the assumption of a constant length scale, L, and is not affected by the large uncertainty in the value of L determined in Sec. V C. It is interesting to note that at the highest Reynolds number the rms acceleration is about 300 m/s^2, or more than 30 times the acceleration of gravity.

Figure 12 shows a_0 calculated from Eq. (24) for the data in Fig. 11(B). Also shown is the direct numerical simulation data from Yeung and Pope[4] and the extrapolation of the $R_\lambda^{1/2}$ scaling they observed. Yeung's recent simulations continue to follow the $R_\lambda^{1/2}$ trend up to $R_\lambda = 200$, where $a_0 = 3$.[15] Particle settling problems prevented us from studying lower Reynolds numbers and directly comparing with the simulation results.

The central feature of Fig. 12 is that the measured value of a_0 is approximately independent of Reynolds number, particularly for the lower noise y data for both particle sizes. From this we conclude that the $R_\lambda \gtrsim 1000$, a_0 has turned over from the $R_\lambda^{1/2}$ scaling previously observed in DNS to showing relatively good agreement with the Kolmogorov ('41) prediction that a_0 is constant. Modest deviations from the Kolmogorov ('41) scaling could lie within the scatter of the data. Further measurements, particularly of the higher moments of the acceleration distribution will be necessary to gain insight into what effects intermittency may have on Lagrangian acceleration statistics.

When interpreting Fig. 12, it is important to recognize that there is a significant uncertainty in the overall scaling of the vertical axis for the measured data which results from the uncertainty in the mean dissipation, or equivalently from the uncertainty in L. This does not affect the conclusion that a_0 is independent of Reynolds number, but it does affect attempts to interpolate between our data and the DNS data. No clear anisotropy between the x and y measurements can be identified, although the larger measurement errors in the x data make this difficult to determine.

The value of the Kolmogorov constant, a_0, is read from Fig. 12 to be 7.0 ± 1.0, where this uncertainty reflects fluctuations between data sets. In addition there is the larger uncertainty in the value $L = 0.21 \pm 0.06$ m which entered into the calculation of each a_0. When added in quadrature these together produce an uncertainty of $\pm 45\%$. Thus the final value of a_0 was found to be 7 ± 3.

Surprisingly, we observed very little difference between the data for the 250 μm particles and the 460 μm particles. This observation supports the hypothesis that the particles, with diameters ranging from 5 up to 25 times the Kolmogorov microscale, were acting like fluid particles to within the accuracy of the measurements. The slight decrease of the data at the highest Reynolds number might be a particle size effect, but this is unclear. The insensitivity to particle size may be related to the fact that the pressure term in the Navier–Stokes equation is dominant in determining the fluid particle acceleration at large Reynolds numbers.

Figure 13 shows the PDF of the measured y acceleration normalized by the rms acceleration from Fig. 11(B) for runs 4, 9, and 11. Tracks are included in the PDF if their tracking time is more than 60% of the maximum tracking time. The logarithmic plot shows exponential tails, suggesting intermittency. No clear deviation between the different Reynolds numbers is observed, particularly when one recognizes the uncertainties in the rms values used for normalization. Although values of the flatness and higher order moments are not reported due to limited statistics and sensitivity to the

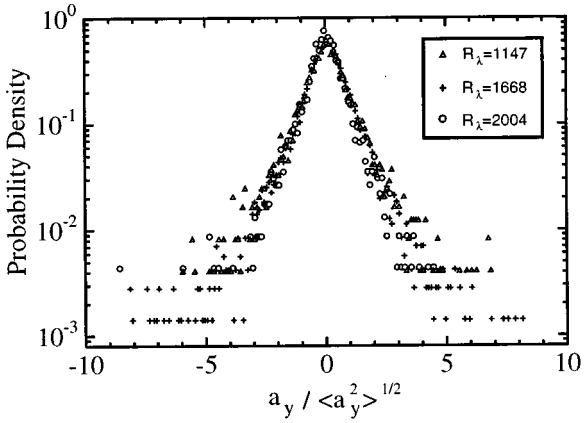

FIG. 13. Probability density function for the *y* acceleration normalized by the rms acceleration [from Fig. 11(B)].

identification of spurious tracks, the flatness is clearly larger than the Gaussian value of 3. The rare events, with accelerations up to eight times the rms were not spurious. For example, the track shown in Fig. 3 is a $R_\lambda = 1668$ and has $a_y / \langle a_y^2 \rangle^{1/2} = 8.2$ which is far in the tail of the plotted PDF.

VII. CONCLUSIONS

In this paper we presented experimental particle tracking measurements in a flow between counter-rotating disks for Taylor Reynolds numbers $900 < R_\lambda < 2000$, an order of magnitude higher than previously possible. We recorded particle tracks by imaging tracer particles onto a position sensitive photodiode, and obtained data with sufficient spatial and temporal resolution to measure accelerations. A primary conclusion is that experimental measurements of Lagrangian quantities at these Reynolds numbers are possible. We have developed a model for correcting particle tracking velocity measurements when residence times are unavailable. We reported results for the acceleration variance which are in good agreement with Kolmogorov's ('41) scaling predictions. These data represent the first validation of the expectation that at large Reynolds numbers Lagrangian accelerations can be described by Kolmogorov ('41) scaling. The scatter in the data does not allow conclusions about possible intermittency corrections to the Kolmogorov ('41) scaling. The value of the Kolmogorov constant for the acceleration variance was found to be 7 ± 3.

ACKNOWLEDGMENTS

We thank S. Pope, E. Siggia, Z. Warhaft, and D. Egolf for many fruitful discussions. We also benefited greatly from discussions with J. Alexander, who pointed out some methods of statistical data analysis developed for high energy physics experiments that can be helpful in guiding the analysis of turbulence data. We thank J. Dobbins from the Laboratory of Nuclear Studies for his contribution to the building of the analog signal processing circuit, and G. Miller from C. Williamson's group for help in obtaining tracer particles. This work was supported by a Cottrell Scholar Award of Research Corporation and NSF Grant No. Phy 9722128. G. V. acknowledges support from the National Science Foundation graduate fellowship program. E. B. acknowledges support from the Alfred P. Sloan Foundation.

[1] G. I. Taylor, ''Diffusion by continuous movements,'' Proc. London Math. Soc. **20**, 196 (1921).
[2] S. B. Pope, ''PDF methods for turbulent reactive flows,'' Prog. Energy Combust. Sci. **11**, 119 (1985).
[3] J. C. Weil, R. I. Sykes, and A. Venkatram, ''Evaluating air-quality models: review and outlook,'' J. Clim. **31**, 1121 (1992).
[4] P. K. Yeung and S. B. Pope, ''Lagrangian statistics from direct numerical simulations of isotropic turbulence,'' J. Fluid Mech. **207**, 531 (1989).
[5] M. Nelkin, ''Universality and scaling in fully developed turbulence,'' Adv. Phys. **43**, 143 (1994).
[6] A. N. Kolmogorov, ''The local structure of turbulence in incompressible viscous fluid for very large Reynolds numbers,'' Dokl. Akad. Nauk SSSR **30**, 301 (1941).
[7] A. S. Monin and A. M. Yaglom, *Statistical Fluid Mechanics*, edited by J. L. Lumley (MIT Press, Cambridge, MA, 1975), Vol. 2.
[8] D. J. Shlien and S. Corrsin, ''A measurement of Lagrangian velocity autocorrelation in approximately isotropic turbulence,'' J. Fluid Mech. **62**, 255 (1974).
[9] W. H. Snyder and J. L. Lumley, ''Some measurements of particle velocity autocorrelation functions in a turbulent flow,'' J. Fluid Mech. **48**, 41 (1971).
[10] Y. Sato and K. Yamamoto, ''Lagrangian measurement of fluid-particle motion in an isotropic turbulent field,'' J. Fluid Mech. **175**, 183 (1987).
[11] M. Virant and T. Dracos, ''3D PTV and its applications on Lagrangian motion,'' Meas. Sci. Technol. **8**, 1539 (1997).
[12] A. M. Obukhov and A. M. Yaglom, ''The microstructure of turbulent flow,'' Prikl. Mat. Mekh. **15**, 3 (1951) [translated in National Advisory Committee for Aeronautics (NACA), TM 1350, Washington, DC (1953)].
[13] G. K. Batchelor, ''Pressure fluctuations in isotropic turbulence,'' Proc. Cambridge Philos. Soc. **47**, 359 (1951).
[14] R. J. Hill and J. M. Wilczak, ''Pressure structure functions and spectra for locally isotropic turbulence,'' J. Fluid Mech. **296**, 247 (1995).
[15] P. K. Yeung, ''Similarity scaling of acceleration and pressure statistics in numerical simulations of isotropic turbulence,'' Phys. Fluids (submitted).
[16] R. J. Hill and S. T. Thoroddsen, ''Experimental evaluation of acceleration correlations for locally isotropic turbulence,'' Phys. Rev. E **55**, 1600 (1997).
[17] S. R. Hanna, ''Lagrangian and Eulerian time-scale relations in the daytime boundary layer,'' J. Appl. Meteorol. **20**, 242 (1981).
[18] K. D. Squires and J. K. Eaton, ''Lagrangian and Eulerian statistics obtained from direct numerical simulations of homogeneous turbulence,'' Phys. Rev. A **3**, 130 (1991).
[19] P. K. Yeung, ''Direct numerical simulation of two-particle relative diffusion in isotropic turbulence,'' Phys. Fluids **6**, 3416 (1994).
[20] P. K. Yeung, ''One- and two-particle Lagrangian acceleration correlations in numerically simulated homogeneous turbulence,'' Phys. Fluids **9**, 2981 (1997).
[21] S. Douady, Y. Couder, and M. E. Brachet, ''Direct observation of the intermittency of intense vorticity filaments in turbulence,'' Phys. Rev. Lett. **67**, 983 (1991).
[22] J. Maurer, P. Tabeling, and G. Zocchi, ''Statistics of turbulence between two counterrotating disks in low-temperature helium gas,'' Europhys. Lett. **26**, 31 (1994).
[23] F. Belin, J. Maurer, P. Tabeling, and H. Willaime, ''Observation of intense filaments in fully developed turbulence,'' J. Phys. II **6**, 573 (1996).
[24] O. Cadot, S. Douady, and Y. Couder, ''Characterization of the low-pressure filaments in a three- dimensional turbulent shear flow,'' Phys. Fluids **7**, 630 (1995).
[25] S. Fauve, C. Laroche, and B. Castaing, ''Pressure fluctuations in swirling turbulent flows,'' J. Phys. II **3**, 271 (1993).
[26] J. Jimenez, A. Wray, P. Saffman, and R. Rogallo, ''The structure of intense vorticity in isotropic turbulence,'' J. Fluid Mech. **255**, 65 (1993).
[27] *CRC Handbook of Chemistry and Physics*, 78th ed., edited by D. R. Lide (CRC, New York, 1997).
[28] P. Buchave, W. K. George, and J. L. Lumley, ''The measurement of turbulence with the laser-Doppler anemometer,'' Annu. Rev. Fluid Mech. **11**, 443 (1979).
[29] J. K. Lindsey, *Parametric Statistical Inference* (Clarendon, Oxford, 1996).

[30]A. Noullez, W. G. Wallace W. Lempert, R. B. Miles, and U. Frisch, ''Transverse velocity increments in turbulent flow using the RELIEF technique,'' J. Fluid Mech. **339**, 287 (1997).
[31]S. Garg and Z. Warhaft, ''On the small scale structure of simple shear flow,'' Phys. Fluids **10**, 662 (1998).
[32]J. R. Taylor, *An Introduction to Error Analysis* (University Science Books, Sausalito, CA, 1997).
[33]M. P. Wand and M. C. Jones, *Kernel Smoothing* (Chapman and Hall, London, 1995).
[34]B. L. Sawford, ''Reynolds number effects in Lagrangian stochastic models of turbulent dispersion,'' Phys. Fluids A **3**, 1577 (1991).
[35]S. B. Pope, ''Lagrangian PDF methods for turbulent flows,'' Annu. Rev. Fluid Mech. **26**, 23 (1994).
[36]S. B. Pope (private communication).